Supplementary Materials S1: MR signal simulation

The 4D-XCAT phantom was used to simulate the abdominothoracic anatomy of the adult male with the following parameters: 2.5 mm isotropic voxel size, heart rate of 80 BPM, 3.0 cm maximum diaphragm motion, 1.0 cm maximum body surface expansion, and breathing period of 5.0 sec. Phantom volumes were generated at the temporal sampling rate of 5.0 msec. A spherical lesion with a 2.0 cm diameter was added in the right middle lobe. Lesion motion was simulated with a displacement of 2.0 cm in the SI direction, 1.0 cm in the AP direction, and no lateral displacement, as shown in Figure S1.

The raw MR signal was simulated by sampling the Fourier transform of the XCAT phantom along the points defined by the radial trajectories described in the manuscript. For the stack-of-stars trajectory, 650 spokes/stack were used. For the multidimensional golden means trajectory, at total of 26000 spokes were used. The discrete Fourier transform was calculated analytically.

Reconstruction time is primarily driven by the number of spokes and matrix size (i.e. the number of sample points per spoke). In a quad-core workstation with 16 GB of RAM, we find that the most limiting step is the calculation of the density compensation factors. This step takes ~1.5 minutes per breathing phase. However, density compensation factors can be pre-computed for a given sampling function. The time for re-gridding and inverse Fourier transform is ~0.3 minutes per breathing phase.

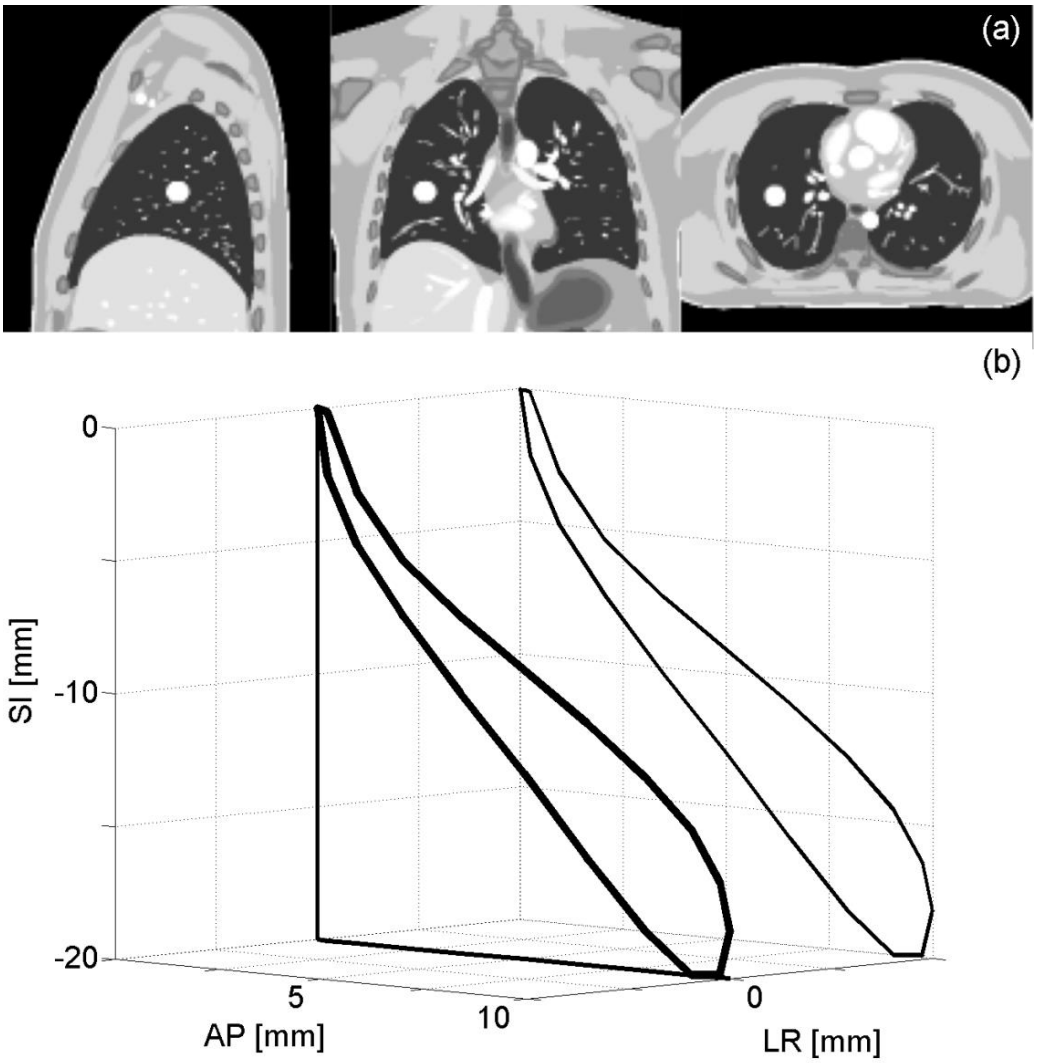

Supplementary Figure S1. (a) Orthogonal slices in the XCAT digital phantom. The 4D-XCAT phantom was used to simulate the abdominothoracic anatomy of the adult male with the following parameters: 2.5 mm isotropic voxel size, heart rate of 80 BPM, 3.0 cm maximum diaphragm motion, 1.0 cm maximum body surface expansion, and breathing period of 5.0 sec. Phantom volumes were generated at the temporal sampling rate of 5.0 msec. **(b)** A spherical lesion with a 2.0 cm diameter was added in the right middle lobe. Lesion motion was simulated with a displacement of 2.0 cm in the SI direction, 1.0 cm in the AP direction, and no lateral displacement. This trajectory is chosen to include motion hysteresis.

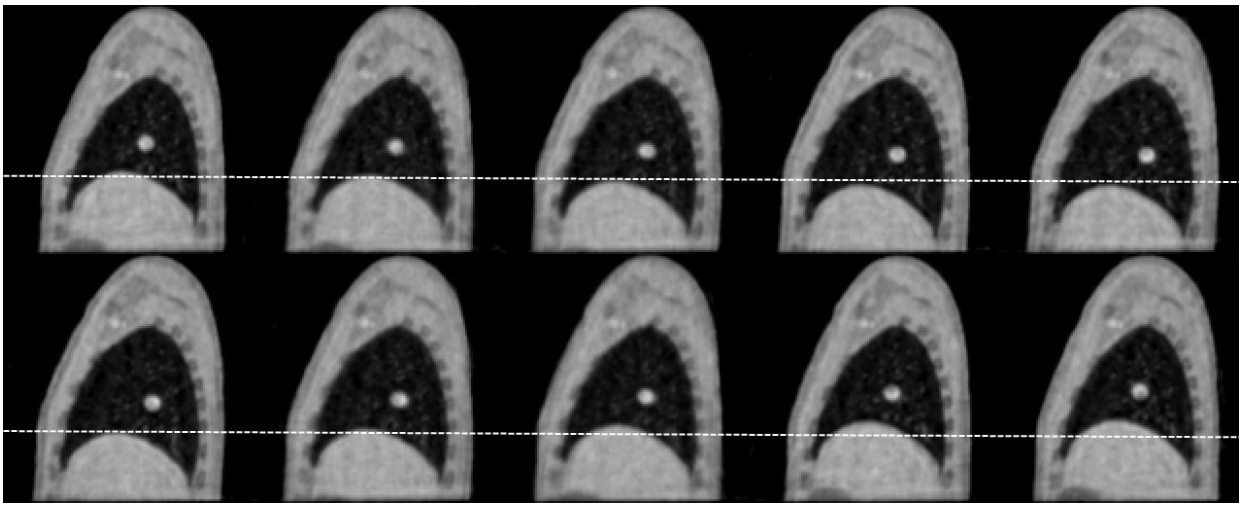

Supplementary Figure S2. Montage of sagittal slices from respiratory phases 1-10 (top row: phases 1-5; bottom row: phases 6-10) reconstructed using RSGR-PEVS.

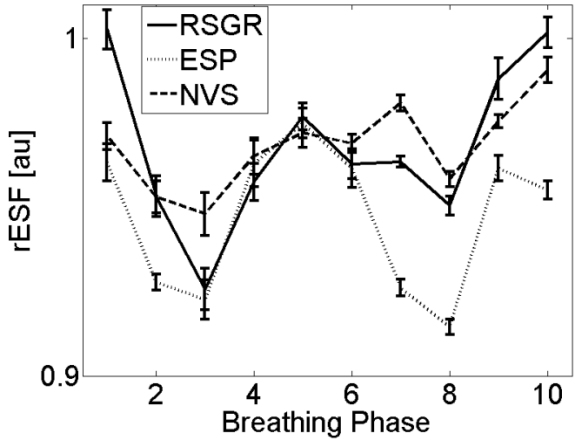

Supplementary Figure S3. Improvements in spatial resolution are respiratory phase dependent. rESF at lung-liver interface as a function of breathing phase for the multidimensional golden means trajectory and the three view-sharing reconstruction techniques described in manuscript.

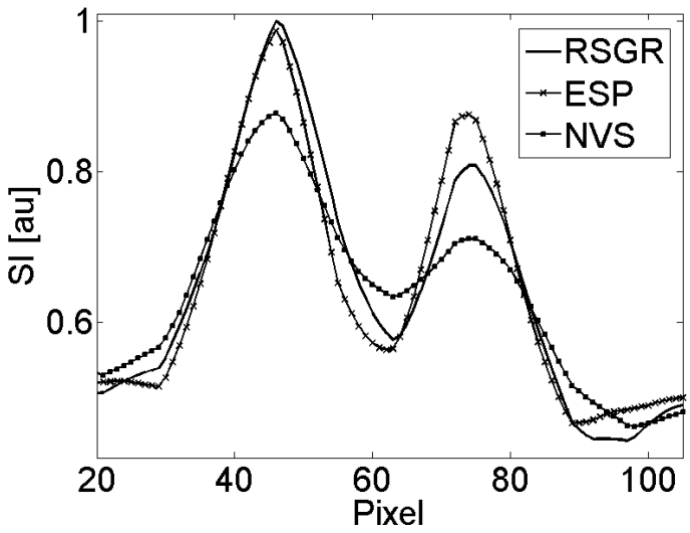

Supplementary Figure S4. Line profiles through pulmonary vessels demonstrating improvements in spatial resolution. The effect of view-sharing is shown for the multidimensional golden means trajectory.

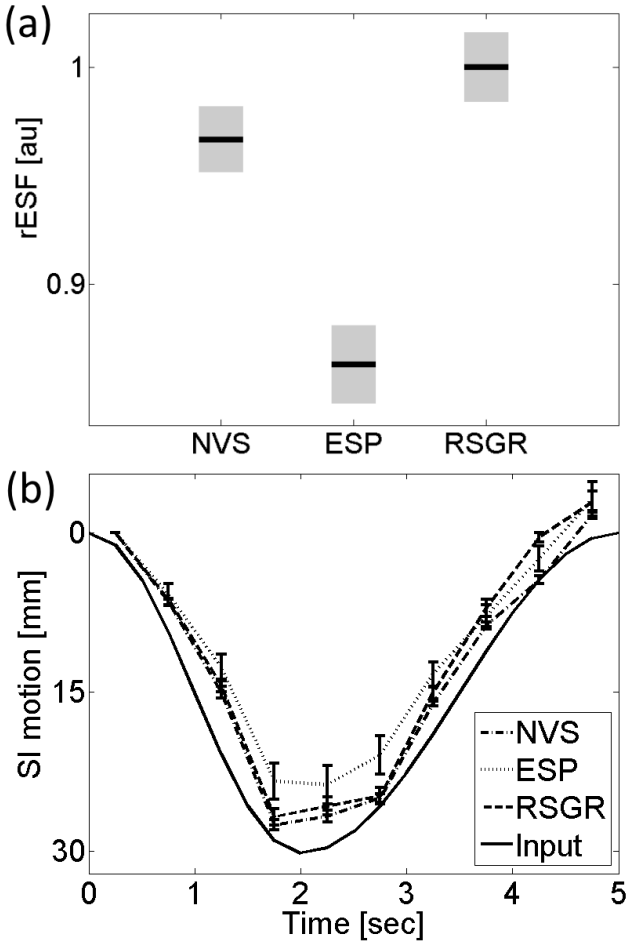

Supplementary Figure S5. Comparison of the effect of view-sharing reconstruction techniques in regions with large temporal changes. (a) Mean rESF across breathing phases as a function of reconstruction technique. In regions with large temporal changes, RSGR-PEVS provides a significant improvement in spatial resolution while ESP-PEVS degrades spatial resolution. Bar-plots depict average ± standard error of mean. (b) Displacement of lung-liver interface determined from ten line profiles at the region highlighted in panel (a). The effect of view-sharing is shown for the multidimensional golden means trajectory.

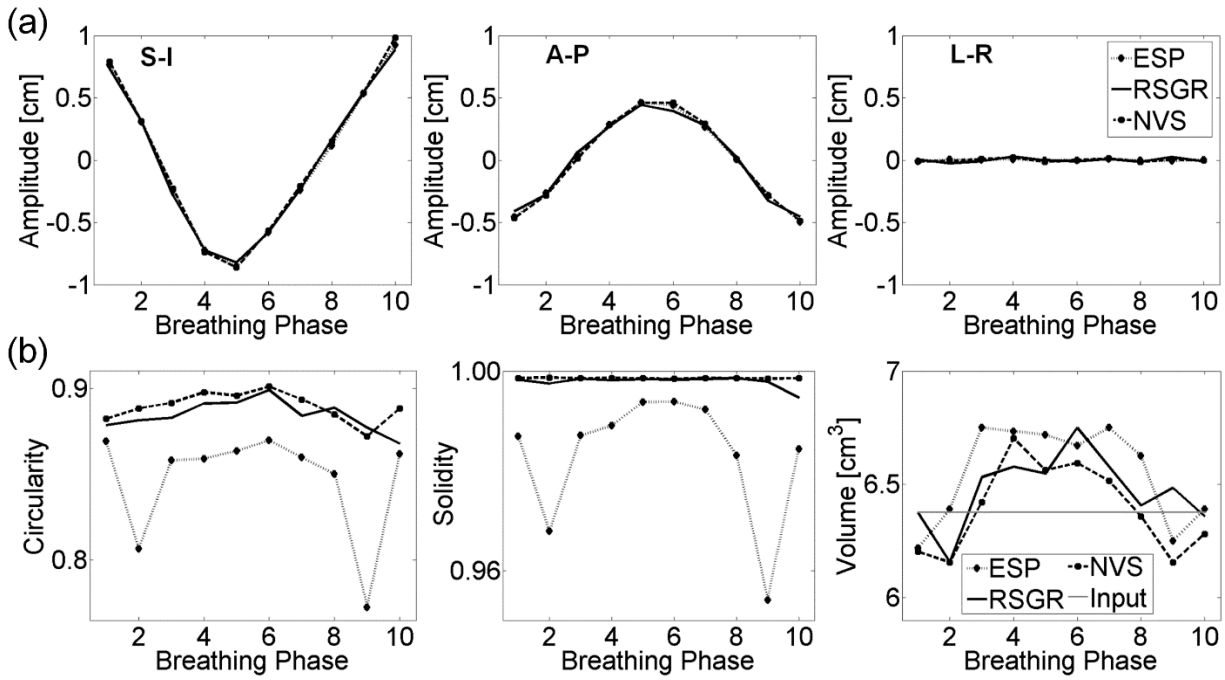

Supplementary Figure S6. Characterization of lesion detection as a function of reconstruction method. (a) Displacement of lesion center-of-mass in (left) superior-inferior (center) anterior-posterior and (right) left-right direction. (b) Shape metrics as a function of respiratory phase: (left) circularity, (center) solidity, and (right) volume of lesion. The effect of view-sharing is shown for the multidimensional golden means trajectory.

Supplementary Materials S2: Imaging parameters for dynamic phantom

The dynamic phantom was imaged in a 7T MR scanner (Bruker BioSpin MRI GmbH, Ettlingen, Germany). An actively detuned volume RF-coil was used in conjunction with a four-channel coil for surface receive. The pulse sequence and acquisition parameters were: gradient-echo, FOV = 30x30x30 mm^3, matrix = 128^3, TR/TE = 5.0/0.02 ms, BW = 100 kHz, NEX = 1, α = 10°, 25200 spokes, and total scan time = 2.1 mins. The respiratory signal was extracted from the center of k-space.

The dynamic phantom was also imaged with Cartesian cine-MRI using the following parameters: FLASH pulse sequence, FOV = 30 mm^3, matrix = 90 x 90, 10 dummy views, single slice imaging, slice thickness = 1 mm, TR/TE = 3.0/1.8 ms, BW = 100 kHz, NEX = 1, α = 10°, and frame rate ~ 3 fps.

The phantom was connected to a linear actuator (Dynamic Phantom, CIRC, Norfolk, VA) able to generate a user-selected trajectory. A sinusoidal motion trajectory with a 2.5 mm amplitude (5.0 mm displacement) and a period of 5 seconds guided the displacement of the 2 mm tube. Motion direction was along the longitudinal axis of the large tube. This configuration simulates a small moving target of known dimensions (2 mm tube) next to a stable and stationary structure (15 mm tube).

We include three movies in order to clarify the motion of the dynamic phantom. The file named **DynPhantom_2D_FLASH.avi** shows the acquisition with 2D FLASH. The file named **DynPhantom_RSGR-PEVS.avi** is a movie of the surface rendered RSGR-PEVS acquisition while **DynPhantom_Sagittal_RSGR-PEVS.avi** shows a movie of the sagittal slice shown in Fig. S7 below.

Figure S7 demonstrates improvements in image quality in the dynamic phantom. The effects of reconstruction on resolution and detection are analyzed in an approach analogous to the one used in the digital XCAT phantom. Panel S7(c) compares the location of the center-of-mass of the 2 mm dynamic phantom. The three 4D-PEVS methods can determine the location

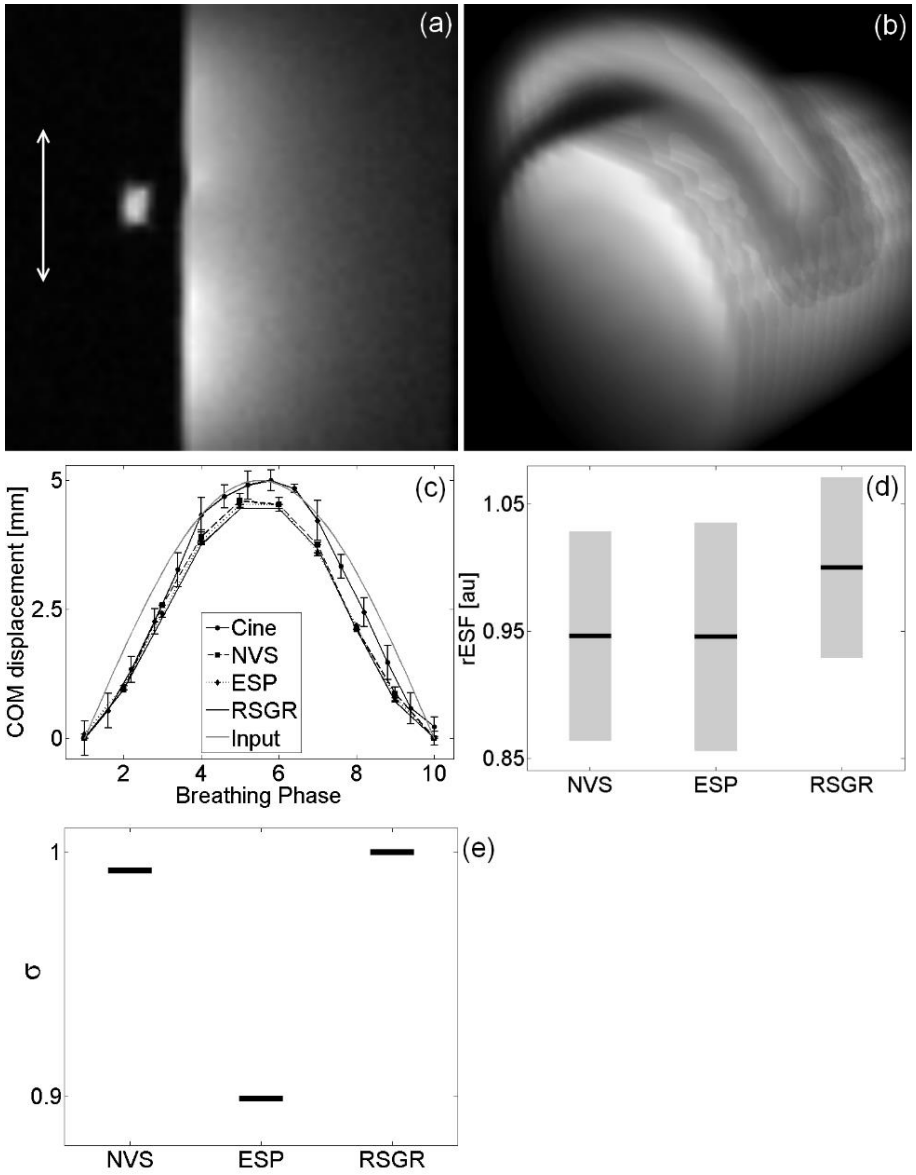

Supplementary Figure S7. Image quality as a function of reconstruction method in a dynamic phantom. **(a)** Sagittal slice at center of phantom (arrow demonstrates direction of motion) and **(b)** surface rendering of phantom image at respiratory phase 1. **(c)** Displacement of phantom center-of-mass as a function of breathing phase. **(d)** Mean rESF (across breathing phases) over moving phantom as a function of reconstruction technique. In regions with large temporal changes RSGR-PEVS provides a significant improvement in spatial resolutions while ESP-PEVS does not improve resolution. Bar-plots depict average ± standard error of mean. **(e)** Effect of reconstruction technique on noise. The noise floor (σ) is estimated by the standard deviation of signal intensity (across phases) in a large background region with no NMR signal.

of the center-of-mass with comparable accuracy. Spatial resolution improvements in features with large temporal changes were assessed by calculating rESF in the moving phantom. rESF

was estimated as the mean image gradient in an ROI enclosing the moving phantom. Mean rESF was significantly higher in images reconstructed with RSGR-PEVS; no significant difference was observed in images reconstructed with ESP-PEVS and NVS-PEVS, as shown in Fig. S7(d). This finding confirms the hypothesis that the average breathing signal is a measure of spatial changes across respiratory phases and can accordingly adapt the amount of data sharing to minimize spatiotemporal blurring. Similar to results observed in the XCAT phantom, further examination of the rESF shows that spatial resolution also varies across breathing phases, as shown in Fig. S8 below. The circularity and solidity of the moving phantom were not significantly different in images reconstructed with any of the 4D-PEVS methods. Finally, a comparison of the noise floor reveals that while ESP-PEVS improves SNR, RSGR-PEVS has a negligible effect on SNR, as shown in Fig. S7(e).

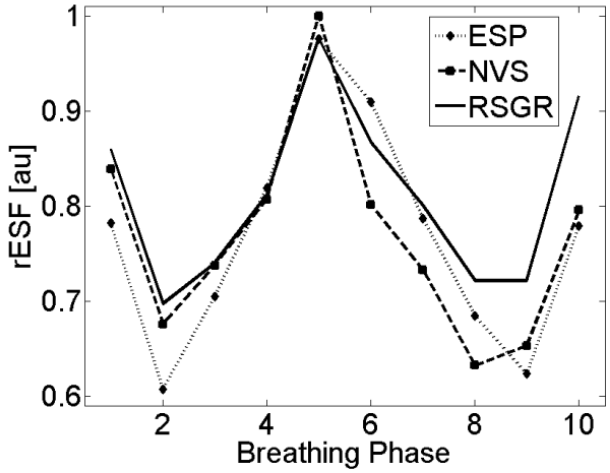

Supplementary Figure S8. rESF in dynamic phantom as a function of breathing phase for the three reconstruction techniques described in manuscript. Improvements in spatial resolution are respiratory phase dependent.

Supplementary Materials S3. Imaging parameters for human volunteer experiments

Study 1

The method was tested in a 3.0T clinical scanner (Verio, Siemens AG, Erlangen, Germany). An actively detuned volume RF-coil was used in conjunction with a 12-channel coil for surface receive. The stack-of-stars sampling function was used with the following acquisition parameters: FOV = 38.4 x 38.4 x 25.6 cm^3, matrix size = 256 x 256, 64 stacks in the k_z-direction (superior-inferior), 650 spokes/stack, TR/TE = 4.06/1.68 ms, BW = 618 Hz/pixel, NEX = 1, α = 12°, and total scan time ~ 2.5 mins. This scan was added to the end of a clinical exam that used 10 ml of Gd-DTPA (Magnevist, Bayer Healthcare, Leverkusen, Germany) followed by a 20-ml saline flush, both injected at a rate of 2 ml/second. The respiratory signal was extracted from projections along the z-direction using principal component analysis, as previously described [1, 2]. The respiratory cycle was retrospectively sorted into ten equal phases based on the phase angle of the breathing signal.

Study 2

The method was tested in a 1.5T clinical scanner (GE Healthcare, Waukesha, WI). An actively detuned receive chest coil (Clinical MR Solutions, Brookfield, WI) was used in conjunction with the body coil for excitation. The multidimensional golden-means sampling function was used with the following acquisition parameters: FOV = 40 cm^3, matrix size = 128^3, TR/TE = 5.0/0.264 ms, BW = 31.25 kHz, NEX = 1, α = 10°, 25000 spokes, and total scan time = 2.1 mins. Breathing motion was monitored with a respiratory bellows belt and compared to the respiratory signal extracted from the DC-component in k-space. The respiratory cycle was retrospectively sorted into ten equal phases based on the phase angle of the breathing signal derived from k-0.

Figure S9 displays a montage of respiratory phase 1, 4, and 8 reconstructed with and without view-sharing. The improvements in spatial resolution can be appreciated at the interface of low-high contrast regions and small features, such as the hepatic vessels. The mean rESF across breathing phases reveals that the degree of blurring in moving edges reconstructed with

RSGR-PEVS is comparable to that found in images reconstructed without view-sharing, as seen in panel S10(a). This finding confirms the hypothesis that the average breathing signal is a

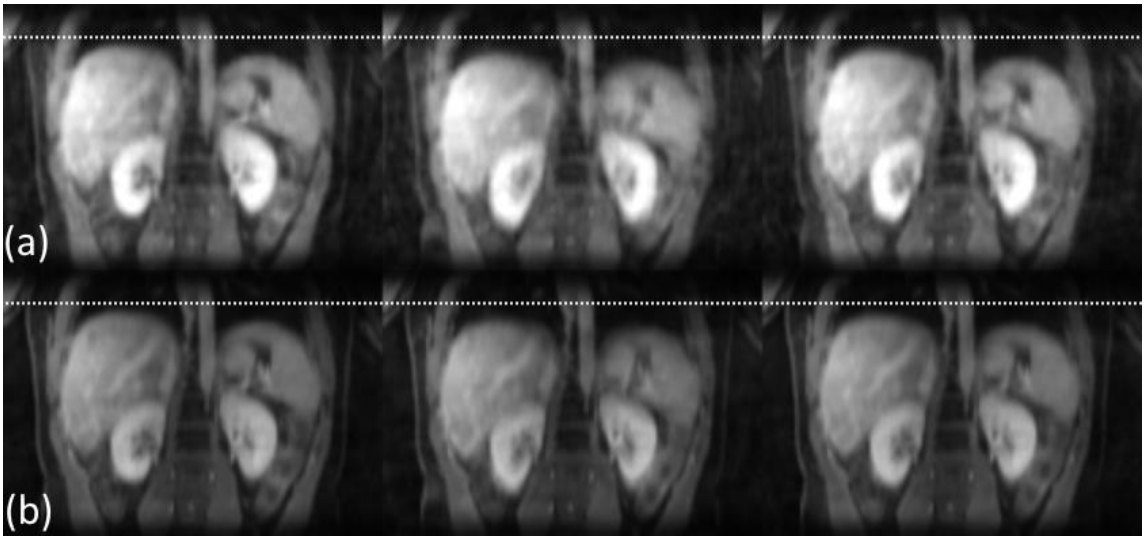

Supplementary Figure S9. Validation in human volunteer at 3.0T. From left to right, phases 1, 4, and 8 from reconstruction **(a)** without and **(b)** with view-sharing. The images are normalized by maximum value of reconstructed intensity and displayed using equal window/level settings. Improvements in spatial resolution can be seen at the lung-liver interface and hepatic vessels.

measure of spatial changes across respiratory phases and can accordingly adapt the amount of data sharing to minimize spatiotemporal blurring. A comparison of the noise floor in images reconstructed with each method reveals that RSGR-PEVS does not degrade SNR, as seen in panel S10(b). Figure S11 shows the respiratory signal determined from principal component analysis of projections in the z-direction.

We include three movies from the volunteer in Study 1 above. The movies display the reconstructions with NVS, ESP, and RSGR (from left to right) in the three cardinal planes.

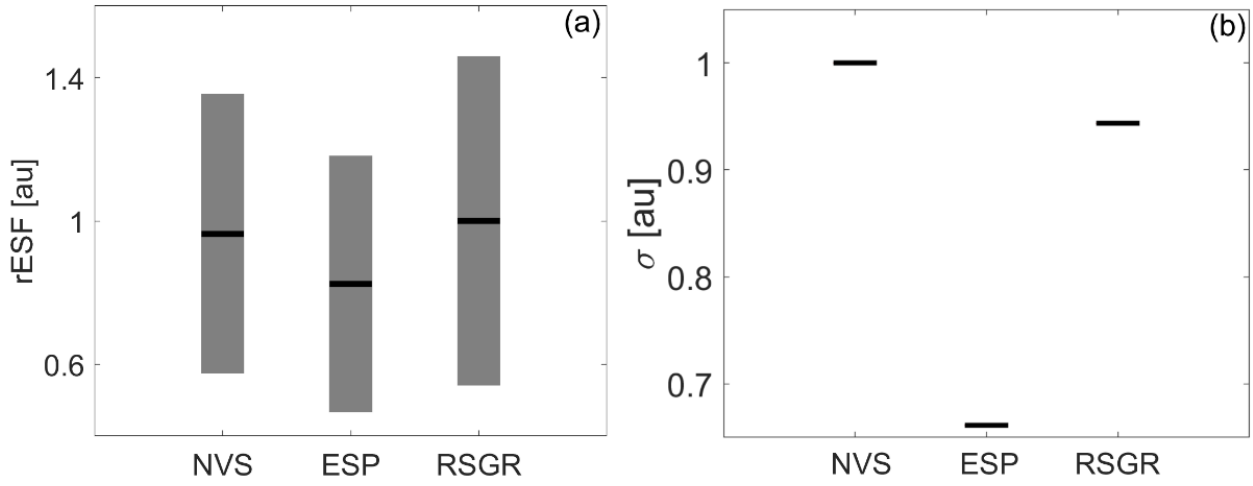

Supplementary Figure S10. (a) Comparison of mean and standard error of rESF calculated at the lung-liver interface in human volunteer scanned at 1.5T using the multidimensional golden means trajectory. The mean and standard error were calculated over ten breathing phases. **(b)** Effect of reconstruction technique on noise. The noise floor (σ) is estimated by the standard deviation of signal intensity (across phases) in a large background region with no NMR signal.

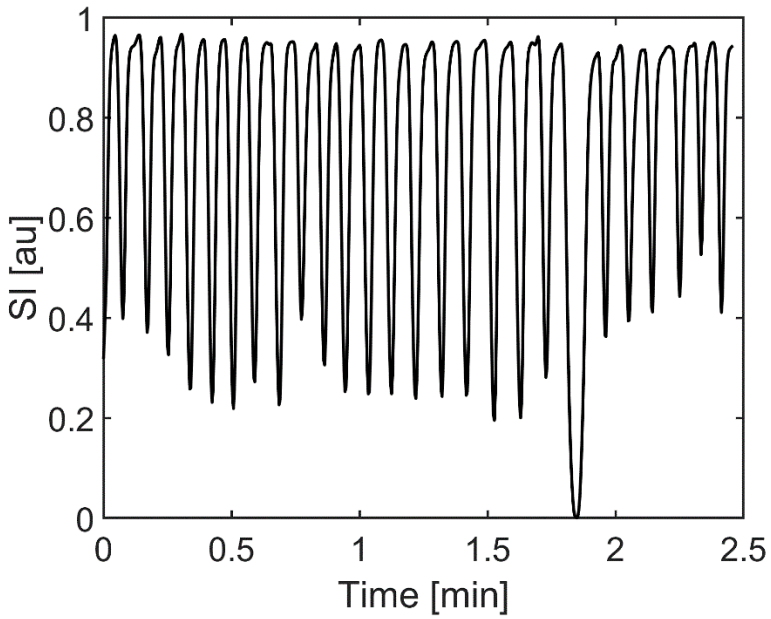

Supplementary Figure S11. Respiratory signal from volunteer in Study 1 described above. Signal determined from principal component analysis of projections in the z-direction.

Figure S12 displays a montage of respiratory phases 1, 4, and 8 reconstructed with and without view-sharing. The improvements in spatial resolution can be appreciated at the interface of low-high contrast regions and small features such as the pulmonary vessels. The mean rESF across breathing phases reveals that the degree of blurring in moving edges reconstructed with RSGR-PEVS is comparable to that found in images reconstructed without view-sharing, as seen in panel S13(a). This finding confirms the hypothesis that the average breathing signal is a

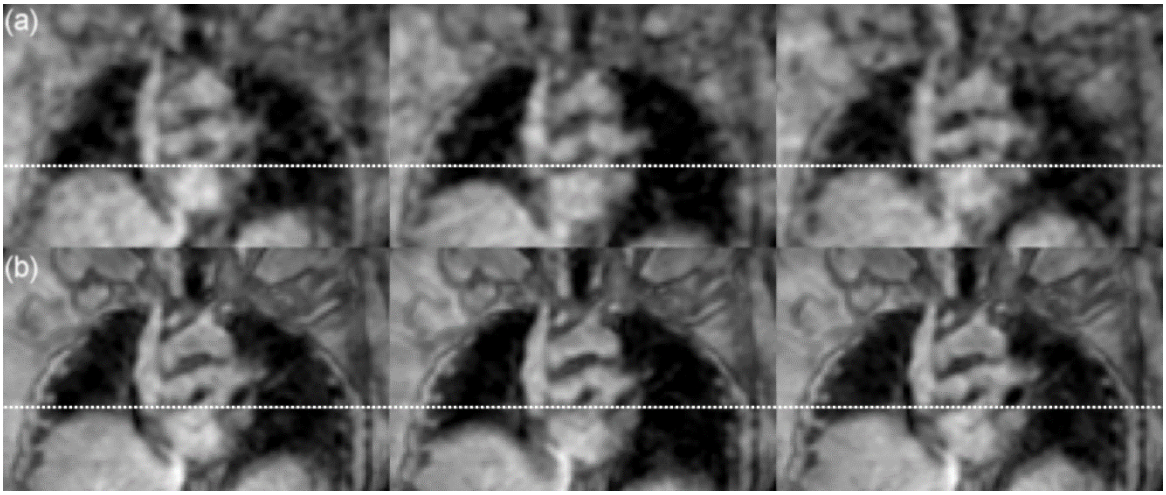

Supplementary Figure S12. Validation in human volunteer at 1.5T. From left to right, phases 1, 4, and 8 from reconstruction **(a)** without and **(b)** with view-sharing. Improvements in spatial resolution can be appreciated at the lung-liver interface and pulmonary vessels. Note that total acquisition time is 2.1 mins.

measure of spatial changes across respiratory phases and can accordingly adapt the amount of data sharing to minimize spatiotemporal blurring. A comparison of the noise floor in images reconstructed with each method reveals that RSGR-PEVS does not degrade SNR, as shown in panel S13(b). Figure S14 shows the respiratory signal determined from the center of k-space.

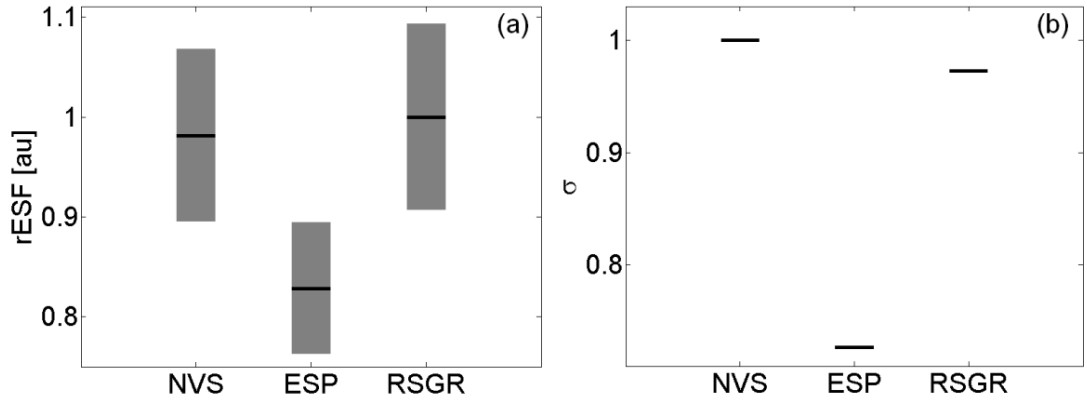

Supplementary Figure S13. (a) Comparison of mean and standard error of rESF calculated at the lung-liver interface in human volunteer. The mean and standard error were calculated over ten breathing phases. **(b)** Effect of reconstruction technique on noise. The noise floor (σ) is estimated by the standard deviation of signal intensity (across phases) in a large background region with no NMR signal. Note that total acquisition time is 2.1 mins.

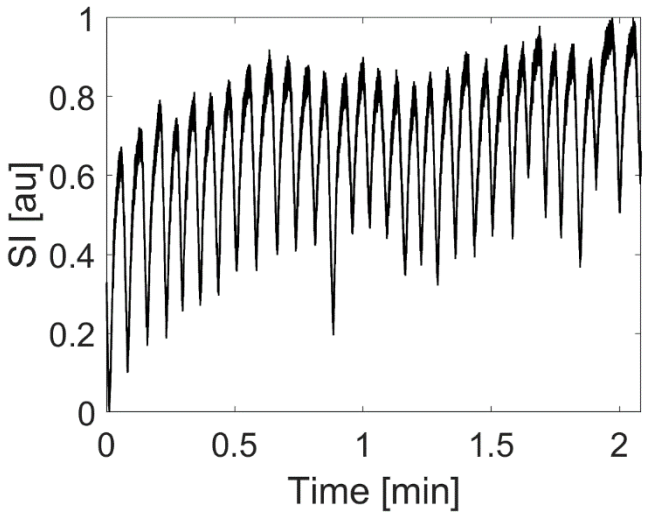

Supplementary Figure S14. Respiratory signal from volunteer in Study 2 described above. Respiratory signal determined from the center of k-space.

REFERENCES

[1] Feng L, Axel L, Chandarana H, Block KT, Sodickson DK, Otazo R. XD-GRASP: Golden-angle radial MRI with reconstruction of extra motion-state dimensions using compressed sensing. Magn Reson Med. 2016;75:775-88.

[2] Feng L, Huang C, Shanbhogue K, Sodickson DK, Chandarana H, Otazo R. RACER-GRASP: Respiratory-weighted, aortic contrast enhancement-guided and coil-unstreaking golden-angle radial sparse MRI. Magn Reson Med. 2018;80:77-89.